nature physics

Article

https://doi.org/10.1038/s41567-023-02102-7

Demonstration of three- and four-body interactions between trapped-ion spins

Received: 14 September 2022

Accepted: 16 May 2023

Published online: 29 June 2023

Check for updates

Or Katz[1,2,3] ✉, Lei Feng[1,2,3] ✉, Andrew Risinger[4], Christopher Monroe[1,2,3,5] & Marko Cetina[1,2,3]

Quantum processors use the native interactions between effective spins to simulate Hamiltonians or execute quantum gates. In most processors, the native interactions are pairwise, limiting the efficiency of controlling entanglement between many qubits. The capability of manipulating entanglement generated by higher-order interactions is a key challenge for the simulation of many Hamiltonian models appearing in various fields, including high-energy and nuclear physics, as well as quantum chemistry and error correction applications. Here we experimentally demonstrate control over a class of native interactions between trapped-ion qubits, extending conventional pairwise interactions to a higher order. By exploiting state-dependent squeezing operations, we realize and characterize high-fidelity gates and spin Hamiltonians comprising three- and four-body spin interactions. Our results demonstrate the potential of high-order spin interactions as a toolbox for quantum information applications.

Useful quantum computers and simulators rely on the controllable generation of quantum entanglement between their elementary constituents, such as qubits or effective spins. Such entanglement allows the efficient exploration of a large state space, which can speed up the computation of certain problems[1] or the simulation of the dynamics or phases of model physical systems[2,3]. The generation of entanglement relies on the native interactions between subsets of spins, which in most quantum platforms is pairwise[4–6]. However, higher-order interactions are often featured in Hamiltonian models in nuclear and high-energy physics[7–10] and spin systems[11–15], as well as quantum circuits and algorithms in quantum chemistry[16–20], error correction codes[21,22] and other applications[23–29]. Sequential or parallel application of universal one- and two-body gate sets can, in principle, generate any unitary mapping in Hilbert space that is equivalent to evolution under high-order interactions[1]. Yet, such constructions carry a large overhead in the number of Trotterization steps[30] or entangling operations[31], thereby limiting the practical performance of such an approach in the presence of decoherence and noise.

From a fundamental view, few-body (>2) interactions can lead to qualitatively different behaviours compared with pairwise interactions, as seen across different fields of physics[32–34]. The study and search for N-body interactions has, thus, become a central research avenue in most quantum platforms, from neutral atoms[35–40] and superconducting systems[39,41–44] to chains of trapped atomic ions[25,27,45–48]. Yet, for trapped-ion processors, which feature dense and controllable qubit connectivity through phonon modes and very long qubit coherence times, robust tunable and scalable interactions beyond the pairwise limit have never been demonstrated.

Here we demonstrate a new class of native higher-order interactions between qubits in a trapped-ion quantum processor. To do this, we apply a state-dependent squeezing optical drive, which is a simple extension over the conventional state-dependent displacement used for Mølmer–Sørensen (MS) pairwise gates[4,49,50]. Such squeezing operations have been applied to trapped-ion systems to improve the performance of pairwise gates[51,52]. Here we instead exploit state-dependent squeezing to generate three- and four-body interactions[53,54]. We outline avenues to extend the scheme and highlight its potential use for quantum computation and simulation at larger scales.

[1]Duke Quantum Center, Duke University, Durham, NC, USA. [2]Department of Electrical and Computer Engineering, Duke University, Durham, NC, USA. [3]Department of Physics, Duke University, Durham, NC, USA. [4]Department of Electrical and Computer Engineering, University of Maryland, College Park, MD, USA. [5]IonQ, Inc., College Park, MD, USA. ✉e-mail: or.katz@duke.edu; lei.feng@duke.edu

https://doi.org/10.1038/s41567-023-02102-7

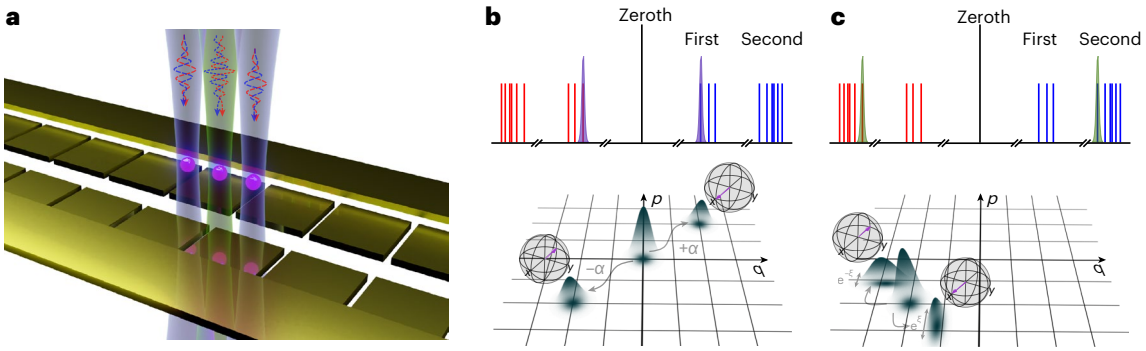

Fig. 1 | Native operations of a trapped-ion quantum processor. a, Linear chain of laser-cooled ion spins in a chip trap. An array of optical beams addressing individual ions enables exquisite control over the state of each spin and its coupling to collective phonon modes using Raman transitions (the additional global beam that forms the Raman pairs is not shown). **b**, Spin-dependent displacement of one phonon mode and its representation over the motional phase space. Simultaneous driving of the first red- and blue-sideband transitions of one ion near resonance with one phonon mode displaces the phonon wavepacket (grey Gaussian) into two distinct trajectories by $\pm\alpha$, depending on the state of that spin along the x direction over its Bloch sphere (purple arrow). **c**, Spin-dependent squeezing of one phonon mode. Simultaneous resonant driving of the second red- and blue-sideband transitions of one ion and one phonon mode squeezes (anti-squeezes) the phonon wavepacket along one direction of phase space by $e^{-\xi}$ (e^{ξ}) depending on the state of that spin along the x direction. **c**, the phonon wavepacket is initially displaced from the origin to illustrate that the squeezing operation scales any initial displacement in a state-dependent manner. The thin lines in **b** and **c** represent the sideband spectrum and narrow purple and green Gaussians represent the spectral content of the Raman coupling near the sidebands.

The quantum processor, operated at the Duke Quantum Center, is based on a chain of $^{171}Yb^{+}$ atomic ions confined in a linear Paul trap on a chip[55–57] (Fig. 1a). Each ion represents a qubit or effective spin comprising two 'clock' levels in its electronic ground-state ($|\uparrow_z\rangle \equiv |F=1, M=0\rangle$ and $|\downarrow_z\rangle \equiv |F=0, M=0\rangle$). We drive motion-sensitive optical Raman transitions on the spin levels using pairs of non-co-propagating beams far detuned from any electronic transitions with a beatnote near the qubit frequency splitting[58]. The spins are initialized and measured using resonant optical pumping and state-dependent fluorescence techniques, resulting in a state preparation and measurement error of <0.5% per ion[59].

The native entangling operations between spins are mediated by phonons and are driven by Raman transitions. The phonons reside in collective modes of motion that feature non-local and dense connectivity with the spins. We simultaneously drive the red- and blue-sideband transitions to displace or squeeze the motional state of ions in selective modes[53]. Driving the first-sideband transitions of the nth ion near the resonance of a single phonon mode generates a spin-dependent displacement $\hat{o}_x^{(n)}\alpha$, where $\hat{o}_x^{(n)}$ is a transverse Pauli matrix and α is the complex displacement parameter. The phonon wavepacket of that mode, represented in the phase space of its harmonic motion[54,60], is therefore displaced by $+\alpha$ if the spin points upwards along the x basis but by $-\alpha$ if the spin points downwards (Fig. 1b; equation (3) provides a mathematical description).

Alternatively, driving the second-sideband transitions of the nth ion at twice the resonance frequency of a single phonon mode squeezes the phonon wavepacket by a factor $e^{\xi\hat{o}_x^{(n)}}$ along the horizontal phonon coordinate q, where ξ is given in equation (6); it is squeezed by a factor $e^{-\xi}$ if the spin points downwards along the x axis, but anti-squeezed by e^{ξ} if the spin points upwards along x (Fig. 1c; equation (5) provides a mathematical description). Temporal control over the amplitudes and phases of the Raman beams over time t enables full control over the magnitudes and phases of both $\alpha(t)$ and $\xi(t)$, respectively, as well as the determination of spin axes of the spin-dependent forces (Methods and refs. 53,54). Crucially, the displacement and squeezing operations depend on the state of the spins, but are independent of the initial phonon state in the Lamb–Dicke regime (when the radial motion along the optical beam is much smaller than the wavelength of the optical drive).

Coupling between different spins is realized by the accumulation of spin-dependent geometric phase Φ that shifts the phase of the quantum state as $|\psi\rangle \to e^{-i\Phi}|\psi\rangle$, similar to the underlying mechanism of the pairwise MS interaction. Here the geometric phase is accumulated by a sequence of alternating displacement and squeezing operations, which move the phonon wavepacket in closed loops in the phase space.

To demonstrate higher-order interactions, we first consider the conventional MS interaction between two ions in a chain of three. Following cooling and spin initialization in the $\left|\downarrow_z^{(1)}\downarrow_z^{(3)}\right\rangle$ state via optical pumping, we drive the lowest-frequency radial phonon mode ('zig-zag' mode) with a sequence of displacement operations that are on resonance with this mode; this sequence alternately acts on the two edge ions (Extended Data Fig. 1a), generating a rectangular-shaped loop in the motional phase space (Fig. 2a)[49]. The accumulated geometric phase corresponds to the phase-space area enclosed in the loop, which is given by $\Phi = \Phi_0\hat{o}_x^{(1)}\hat{o}_x^{(3)}$. We control $\Phi_0 = \alpha^2$ by scaling the amplitude of the displacement pulses and fixing the total duration of the sequence to about 180 μs. We suppress the displacement of other phonon modes by pulse shaping of the displacement waveforms[61] and also suppress the effect of uncompensated level shifts using a pair of echo pulses (Methods). The application of this phase gate jointly flips the spin pair into the state $\left|\uparrow_z^{(1)}\uparrow_z^{(3)}\right\rangle$ with probability $p_{\left(\uparrow_z^{(1)}\uparrow_z^{(3)}\right)} = \sin^2(\Phi_0)$, which is detected via state-dependent fluorescence (Fig. 2a). We determine the scale of Φ_0 by fitting the data in Fig. 2a to a sine-squared function as a function of the Raman beam intensity.

We extend the pairwise interaction by interspersing the sequence squeezing operations that act only on the middle spin and are on resonance with the zig-zag phonon mode (Extended Data Fig. 1b). These operations are realized as pairs of squeezing and anti-squeezing pulses that sandwich the displacement operations (Fig. 2). The squeezing forces scale the momentum displacements by the spin-dependent factor $e^{\xi\hat{o}_x^{(2)}} \equiv \cosh(\xi)\mathbb{1} + \sinh(\xi)\hat{o}_x^{(2)}$, where $\mathbb{1}$ is the identity matrix. The geometric phase is then given by the scaled rectangular area

$$\Phi = \Phi_0\left(\cosh(\xi)\hat{o}_x^{(1)}\hat{o}_x^{(3)} + \sinh(\xi)\hat{o}_x^{(1)}\hat{o}_x^{(2)}\hat{o}_x^{(3)}\right), \quad (1)$$

manifesting two- and three-body interaction terms.

We demonstrate the action of this phase gate (Fig. 2b,c) on the initial states $\left|\downarrow_z^{(1)}\uparrow_x^{(2)}\downarrow_z^{(3)}\right\rangle$ and $\left|\downarrow_z^{(1)}\downarrow_x^{(2)}\downarrow_z^{(3)}\right\rangle$, for a total sequence time of less than 300 μs, including all the displacement, echo and squeezing operations. Similar to the MS interaction, this gate jointly flips the state of the two edge spins, but with probability $P_{\left(\uparrow_z^{(1)}\uparrow_z^{(3)}\right)} = \sin^2(e^{\pm\xi}\Phi_0)$,

https://doi.org/10.1038/s41567-023-02102-7

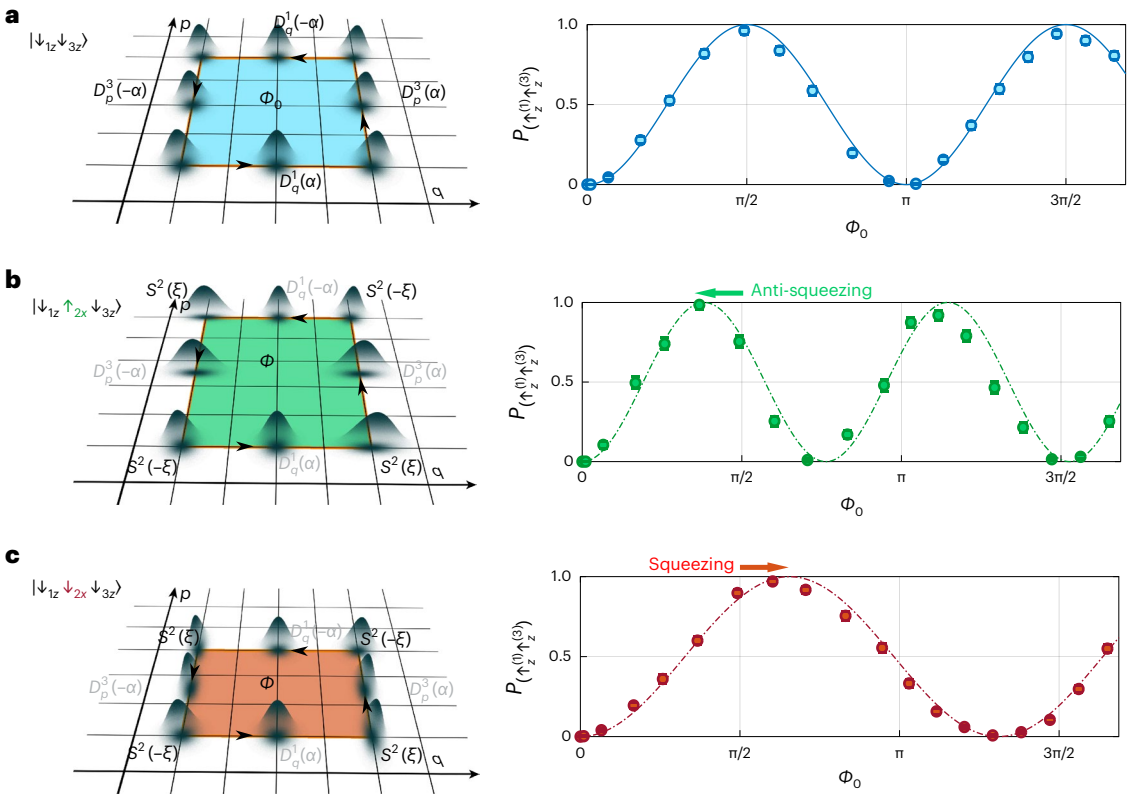

Fig. 2 | Quantum phase gates. a, MS phase gate between ion numbers 1 and 3 using displacement operations of one phonon mode using Milburn's scheme[49] (Fig. 1a). The phase-space area of the enclosed rectangular contour Φ_0 controls the spin evolution, jointly flipping the initial state $\left|\downarrow_z^{(1)}\downarrow_z^{(3)}\right\rangle$ into the state $\left|\uparrow_z^{(1)}\uparrow_z^{(3)}\right\rangle$. Here $D_q^{(n)}(\alpha)$ and $D_p^{(n)}(\alpha)$ denote the momentum and position displacement operations, respectively, applied on the nth ion. **b**,**c**, Interspersing spin-dependent squeezing operations $S^{(2)}(\pm\xi)$ on ion number 2 in between displacement stages along the p coordinate scales the accumulated phase-space area Φ conditioned on the state of that spin (equation (1)). In **a**–**c**, the phonon wavepacket is brought back to its original state at the end of the gate operation to erase the spin–phonon correlations developed during the gate. Measured data (circles) and centre of the error bars are presented as mean values, bars represent 1σ binomial uncertainties, solid line in **a** is a fit to a sine-squared function and dot–dash lines in **b** and **c** are the analytically calculated unitary evolution for the system parameters estimated independently. In **a** and **c** (**b**), each data point is derived from 400 (200) measurements. The applied experimental sequences are presented in Extended Data Fig. 1a,b.

whose dependence on α^2 is scaled by a factor e^{ξ} ($e^{-\xi}$) and is conditioned on the state of the middle spin pointing upwards (downwards) along the x direction. The calculated evolution of $\xi = 0.27$, estimated independently from equation (6) given the applied optical force amplitude, agrees well with the observation.

This many-body entanglement operation features full control over the amplitudes of the two- and three-body terms appearing in equation (1). We can, for example, eliminate the contribution of the two-body term by setting $\Phi_0 = \pi/\cosh\xi$ (because the term $e^{-i\pi\hat{\sigma}_x^{(1)}\hat{\sigma}_x^{(3)}} = -\mathbb{1}$ is spin independent) and generate a pure three-body term with amplitude $\pi\tanh\xi$. We note that maximally entangled states between three spins in this case require only 1 dB of squeezing ($\tanh\xi = \frac{1}{4}$) (ref. 53).

We perform a limited characterization of this pure three-body interaction by measuring the output states for each of the eight distinct three-qubit input eigenstates, all in the z basis. The ideal population distributions of the expected states are equal weightings of the two complementary three-qubit states for each input state (Fig. 3a, wire frames). The measured spin population distributions are shown as solid bars in this figure (Supplementary Fig. 4 shows the numerical values), resulting in an average population fidelity of (95.8 ± 0.9)%, uncorrected for state preparation and measurement and single-qubit gate errors. We further study the coherence in this three-body mapping from two particular input states $\left|\downarrow_z^{(1)}\downarrow_z^{(2)}\downarrow_z^{(3)}\right\rangle$ and $\left|\uparrow_z^{(1)}\uparrow_z^{(2)}\uparrow_z^{(3)}\right\rangle$ into the expected Greenberger–Horne–Zeilinger (GHZ) states $\frac{1}{\sqrt{2}}\left(\left|\downarrow_z^{(1)}\downarrow_z^{(2)}\downarrow_z^{(3)}\right\rangle \pm \left|\uparrow_z^{(1)}\uparrow_z^{(2)}\uparrow_z^{(3)}\right\rangle\right)$. We measure the entanglement of these particular GHZ states using the parity fringe witness observable[62] (Fig. 3b), and extract state fidelities $\mathcal{F} = (94.8 \pm 1.5)\%$ and $\mathcal{F} = (94.4 \pm 1.9)\%$, respectively, uncorrected for state preparation and measurement and single-qubit gate errors. We compare these results with an independently calibrated error model (Supplementary Note 1), and find very good agreement. The leading types of error—uncorrelated bit-flip and phase-flip errors—are similar to the errors affecting two-qubit MS gates that are commonly used to create GHZ states[62–64].

The sequence of displacement and squeezing operations can be realized at various laser intensities, providing continuous control over the values of ξ and Φ_0 that can be implemented in equation (1). This control allows gates to be realized that are taken from a continuous set in the form $U(\xi, \Phi_0) = \exp(-i\Phi_0 H_{\text{eff}})$ and are equivalent to the unitary evolution generated by a unitless, effective spin Hamiltonian $H_{\text{eff}}(\xi) = \Phi/\Phi_0$ setting $\hbar = 1$. This equivalence allows the application of gates that can simulate the evolution of spins by the same effective Hamiltonian H_{eff} but for different values of Φ_0 using a single sequence of displacement and squeezing operations, and scaling the amplitude of the beams that displace the edge ions. We demonstrate the evolution by the effective Hamiltonian associated with equation (1) for $\xi = 0.23$ (calculated from equation (6)) and for the initial state $\left|\downarrow_z^{(1)}\downarrow_z^{(2)}\downarrow_z^{(3)}\right\rangle$, presenting the magnetization $\langle\hat{\sigma}_z^{(n)}\rangle$ of each spin (Fig. 4). The observed spin evolution manifests interference effects owing to the interplay

https://doi.org/10.1038/s41567-023-02102-7

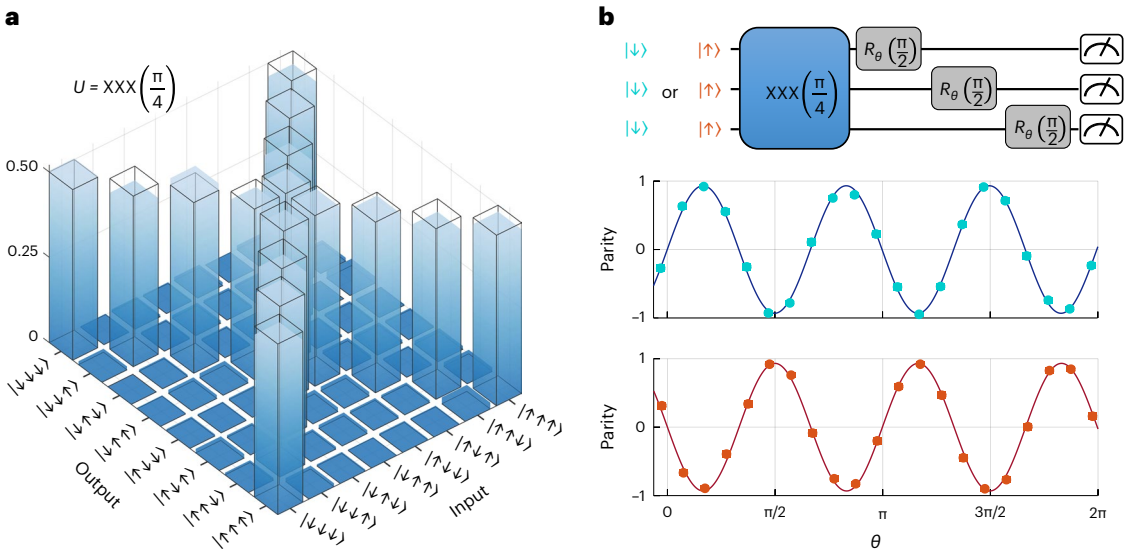

Fig. 3 | Characterization of a three-body interaction gate. a, Truth table of a three-body gate $\mathrm{XXX}(\frac{\pi}{4}) = \exp(-\mathrm{i}\frac{\pi}{4}\hat{\sigma}_x^{(1)}\hat{\sigma}_x^{(2)}\hat{\sigma}_x^{(3)})$ generated by a sequence of displacement and squeezing operations. The input and output spin states are along the z basis. Each input state is ideally mapped into a pair of output states (wire frames), and the raw measurements are shown as the solid bars. The measured populations of these target states are (95.8 ± 0.9)%, averaged over the eight measured configurations. **b**, Characterization of the parity fringe witness observable obtained by the gate. We measure the parity fringe of the output GHZ state for the two initial states $\left|\downarrow_z^{(1)}\downarrow_z^{(2)}\downarrow_z^{(3)}\right\rangle$ (light blue) and $\left|\uparrow_z^{(1)}\uparrow_z^{(2)}\uparrow_z^{(3)}\right\rangle$ (red) with a fitted amplitude of 0.932 ± 0.015 for the two states. The extracted GHZ fidelities for this operation for the two states are $\mathcal{F} = (94.8 \pm 1.5)\%$ and $\mathcal{F} = (94.4 \pm 1.9)\%$. Data and centre of the error bars are presented as mean values, bars represent 1σ binomial uncertainties and each data point is derived from 300 measurements. The solid lines are fitted sine functions. In **b**, the operation $R_\theta(\pi/2)$ denotes single-qubit rotations by azimuthal angle θ and polar angle $\pi/2$ on the Bloch sphere. The measured values are uncorrected for errors in state preparation, measurement and single-qubit rotations.

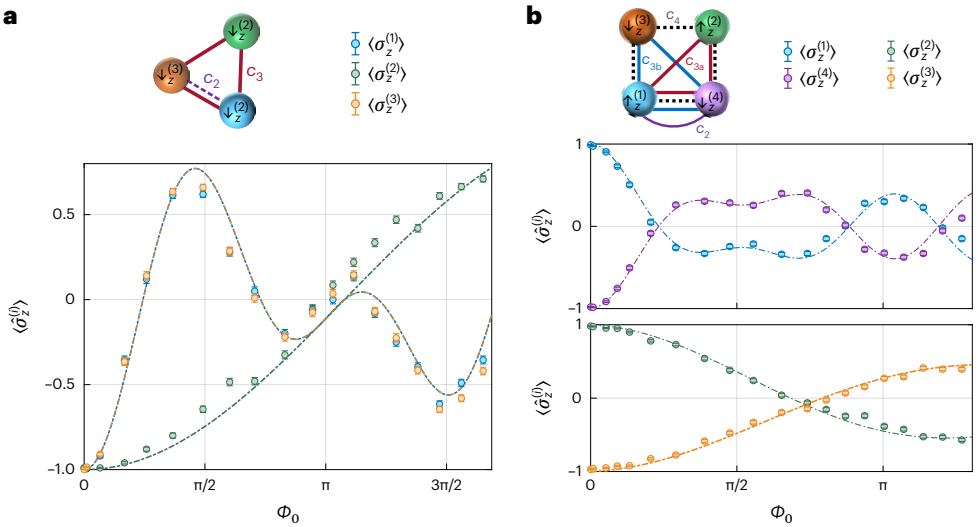

Fig. 4 | Evolution by effective Hamiltonians with three- and four-body interactions. a, Spin magnetization $\langle\hat{\sigma}_z^{(n)}\rangle$ under displacement and squeezing operations (Extended Data Fig. 1b) shown as a function of Φ_0 for the initial state $\left|\downarrow_z^{(1)}\downarrow_z^{(2)}\downarrow_z^{(3)}\right\rangle$. Mathematically, this dynamics is equivalent to the evolution generated by the effective Hamiltonian $H_{\mathrm{eff}} = \Phi/\Phi_0$ for Φ in equation (1). The effective Hamiltonian comprises two- and three-body terms with magnitudes $c_2 = 1.03$ and $c_3 = 0.23$, as illustrated via the links connecting the different spins. Here Φ_0 has the role of the effective evolution time (in units of $\hbar = 1$) and is controlled by the amplitude of the Raman beams (described in the main text). **b**, Evolution of four spins by the displacement and squeezing operations (Extended Data Fig. 1c) for the initial state $\left|\uparrow_z^{(1)}\uparrow_z^{(2)}\downarrow_z^{(3)}\downarrow_z^{(4)}\right\rangle$. The evolution here is equivalent to the one generated by an effective Hamiltonian $H_{\mathrm{eff}} = \Phi/\Phi_0$ for Φ in equation (2) simultaneously containing two-, three- and four-body terms with amplitudes $c_2 = 1.10$, $c_{3a} = 0.36$, $c_{3b} = 0.31$ and $c_4 = 0.10$. The dot–dash lines are the analytically calculated magnetizations for the same initial states where amplitudes c are determined from the calculated squeezing parameters. Data and centre of the error bars are presented as mean values, bars represent 1σ binomial uncertainties and each data point is derived from 400 measurements. Also, Φ_0 is experimentally controlled via scaling the amplitude of the laser beams acting on the edge ions but fixing all the other sequence parameters.

between the two- and three-body terms in the effective Hamiltonian, and is in good agreement with the analytically calculated evolution (Fig. 4, dot–dash lines).

We extend this technique to generate an effective Hamiltonian in a four-ion chain. As in the three-ion gate, we act on two edge ions with displacement operations, whereas the squeezing is simultaneously

performed on the two middle ions, with squeezing parameters ξ and ζ shown in Extended Data Fig. 1c. Unlike the displacement operation that is linear in the spin operators, the total scaling factor of the phonons $e^{\xi\hat{o}_x^{(2)}} e^{\zeta\hat{o}_x^{(3)}}$ is multiplicative in the spin operators, owing to the nonlinear nature of the squeezing operation. Therefore, we realize the geometric phase of the scaled rectangle as

$$\Phi = \Phi_0\Big(c_2\hat{o}_x^{(1)}\hat{o}_x^{(4)} + c_{3a}\hat{o}_x^{(1)}\hat{o}_x^{(2)}\hat{o}_x^{(4)} + c_{3b}\hat{o}_x^{(1)}\hat{o}_x^{(3)}\hat{o}_x^{(4)} + c_4\hat{o}_x^{(1)}\hat{o}_x^{(2)}\hat{o}_x^{(3)}\hat{o}_x^{(4)}\Big), \quad (2)$$

which is equivalent to the effective evolution by Hamiltonian in the form of $H_{\mathrm{eff}}(\xi,\zeta) = \Phi/\Phi_0$. The effective Hamiltonian contains two-, three- and four-body terms whose relative amplitudes are given by $c_2 = \cosh\xi\cosh\zeta$, $c_{3a} = \sinh\xi\cosh\zeta$, $c_{3b} = \cosh\xi\sinh\zeta$ and $c_4 = \sinh\xi\sinh\zeta$. In Fig. 4b, we demonstrate the evolution by this effective Hamiltonian for the initial state $\left|\uparrow_z^{(1)}\uparrow_z^{(2)}\downarrow_z^{(3)}\downarrow_z^{(4)}\right\rangle$ and the applied values $\xi = 0.34$ and $\zeta = 0.29$ (as calculated from equation (6)), following the calibration of Φ_0. The evolution in this case manifests interference between the four different terms in the Hamiltonian, and is in good agreement with the theoretically calculated evolution (Fig. 4b, dot–dash lines).

In summary, we demonstrate a technique to realize native entangling operations comprising higher-order interactions between the spins of trapped ions. Our approach allows engineering new classes of programmable native gates and Hamiltonians using current trapped-ion hardware and requiring only minor alternations in the optical force spectrum and modest levels of squeezing.

It is interesting to compare this approach with the alternative necessary resources of a digital quantum computer using just two-body interactions (and neglecting the cost of single-qubit operations). The approach presented here allows the preparation of effective Hamiltonians comprising families of polynomials of Pauli strings in the x basis whose order is up to the length N of the chain. Owing to the collective nature of the phonon modes that are used as a quantum bus, these polynomials can feature dense connectivity, resulting in many different and non-local interaction terms. This scheme requires a fixed amount of displacement operations (equivalent to several two-qubit gates) and additional squeezing operations that carry a run-time overhead whose relative duration for a fixed optical power grows linearly in N (ref. 53). Given only two-qubit interactions, the construction of a single Pauli string of order $n > 2$ can be realized with $2n$ two-qubit gates or a couple of multiqubit MS gates[1,12,62–64]. A general spin polynomial with commuting terms can be constructed with the sequential application of $\sum_{n=2}^{N}\binom{N}{n}2n$ two-qubit gates, which grows exponentially in N (ref. 31). Although some polynomials can be efficiently constructed with two- or multiqubit MS gates based on two-qubit interactions (where the latter features potential quadratic speedup compared with the former[63–65]), the dramatically different scaling of our approach suggests that the operations presented here can potentially speed up operations in a quantum processor.

The speed of operations in long ion chains is of great importance because at long evolution times, the gate fidelities are affected by correlated noise that originates from motional heating, requiring in-sequence cooling[57]. We note that this gate scheme may enjoy a further improvement in speed by using light ions (for example, $^9Be^+$) with a high Lamb–Dicke parameter η. This is because the speed of spin-dependent squeezing operations scales quadratically with η, whereas spin-dependent displacement operations in conventional gates scale only linearly with η.

This demonstration can be extended to a variety of different sequences that can improve the robustness of the operations and/or construct different sets of spin-entangling operations. For example, the rectangular-shaped loop can be alternatively shaped into other trajectories in the phase space that would render the operation more robust to noise (for example, to frequency drifts of the oscillator) using pulse-shaping techniques[52,66–69]. Furthermore, pulse shaping of the squeezing pulses enables control over the coupling between spins and all the motional modes, despite the density of the second-sideband spectrum, enabling extension of the technique to longer ion chains[54].

Although the displacement and squeezing operations in this demonstration were sequentially executed, on-resonance, simultaneous[53] and/or off-resonance operations[54] can natively realize additional classes of quantum gates and spin Hamiltonians comprising high-order interactions, including pure N-body terms with $N \geq 4$. Other gates with many-body interactions are generally accompanied by other many-body terms of lower order, as demonstrated above (Fig. 4b). The full power and expression of such interactions in trapped-ion quantum computers may, thus, benefit from machine learning approaches[70] to deploy families of such interactions for speeding up and improving the performance of general quantum circuits. It could be particularly useful in variational quantum algorithms[71–73] that can expand the native set of gates.

Online content

Any methods, additional references, Nature Portfolio reporting summaries, source data, extended data, supplementary information, acknowledgements, peer review information; details of author contributions and competing interests; and statements of data and code availability are available at https://doi.org/10.1038/s41567-023-02102-7.

References

1. Nielsen, M. A. & Chuang, I. L. *Quantum Computation and Quantum Information* (Cambridge Univ. Press, 2000).
2. Monroe, C. et al. Programmable quantum simulations of spin systems with trapped ions. *Rev. Mod. Phys.* **93**, 025001 (2021).
3. Feng, L. et al. Continuous symmetry breaking in a trapped-ion spin chain. Preprint at *arXiv* https://doi.org/10.48550/arXiv.2211.01275 (2022).
4. Mølmer, K. & Sørensen, A. Multiparticle entanglement of hot trapped ions. *Phys. Rev. Lett.* **82**, 1835 (1999).
5. Kjaergaard, M. et al. Superconducting qubits: current state of play. *Annu. Rev. Condens. Matter Phys.* **11**, 369–395 (2020).
6. Gross, C. & Bloch, I. Quantum simulations with ultracold atoms in optical lattices. *Science* **357**, 995–1001 (2017).
7. Banuls, M. C. et al. Simulating lattice gauge theories within quantum technologies. *Eur. Phys. J. D* **74**, 165 (2020).
8. Ciavarella, A., Klco, N. & Savage, M. J. Trailhead for quantum simulation of SU(3) Yang-Mills lattice gauge theory in the local multiplet basis. *Phys. Rev. D* **103**, 094501 (2021).
9. Hauke, P., Marcos, D., Dalmonte, M. & Zoller, P. Quantum simulation of a lattice Schwinger model in a chain of trapped ions. *Phys. Rev. X* **3**, 041018 (2013).
10. Farrell, R. C. et al. Preparations for quantum simulations of quantum chromodynamics in 1+1 dimensions: (I) axial gauge. *Phys. Rev. D* **107**, 054512 (2023).
11. Pachos, J. K. & Plenio, M. B. Three-spin interactions in optical lattices and criticality in cluster Hamiltonians. *Phys. Rev. Lett.* **93**, 056402 (2004).
12. Müller, M., Hammerer, K., Zhou, Y., Roos, C. F. & Zoller, P. Simulating open quantum systems: from many-body interactions to stabilizer pumping. *New J. Phys.* **13**, 085007 (2011).
13. Motrunich, O. I. Variational study of triangular lattice spin-1/2 model with ring exchanges and spin liquid state in κ-$(ET)_2Cu_2(CN)_3$. *Phys. Rev. B* **72**, 045105 (2005).
14. Andrade, B. et al. Engineering an effective three-spin Hamiltonian in trapped-ion systems for applications in quantum simulation. *Quantum Sci. Technol.* **7**, 034001 (2022).
15. Bermudez, A., Porras, D. & Martin-Delgado, M. Competing many-body interactions in systems of trapped ions. *Phys. Rev. A* **79**, 060303 (2009).

16. Seeley, J. T., Richard, M. J. & Love, P. J. The Bravyi-Kitaev transformation for quantum computation of electronic structure. *J. Chem. Phys.* **137**, 224109 (2012).
17. O'Malley, P. J. J. et al. Scalable quantum simulation of molecular energies. *Phys. Rev. X* **6**, 031007 (2016).
18. Nam, Y. et al. Ground-state energy estimation of the water molecule on a trapped-ion quantum computer. *NPJ Quantum Inf.* **6**, 33 (2020).
19. Aspuru-Guzik, A., Dutoi, A. D., Love, P. J. & Head-Gordon, M. Simulated quantum computation of molecular energies. *Science* **309**, 1704–1707 (2005).
20. Hempel, C. et al. Quantum chemistry calculations on a trapped-ion quantum simulator. *Phys. Rev. X* **8**, 031022 (2018).
21. Paetznick, A. & Reichardt, B. W. Universal fault-tolerant quantum computation with only transversal gates and error correction. *Phys. Rev. Lett.* **111**, 090505 (2013).
22. Kitaev, A. Y. Fault-tolerant quantum computation by anyons. *Ann. Phys.* **303**, 2–30 (2003).
23. Vedral, V., Barenco, A. & Ekert, A. Quantum networks for elementary arithmetic operations. *Phys. Rev. A* **54**, 147 (1996).
24. Grover, L. K. A fast quantum mechanical algorithm for database search. In *Proc. Twenty-Eighth Annual ACM Symposium on Theory of Computing* 212–219 (ACM, 1996).
25. Wang, X., Sørensen, A. & Mølmer, K. Multibit gates for quantum computing. *Phys. Rev. Lett.* **86**, 3907–3910 (2001).
26. Monz, T. et al. Realization of the quantum Toffoli gate with trapped ions. *Phys. Rev. Lett.* **102**, 040501 (2009).
27. Arias Espinoza, J. D., Groenland, K., Mazzanti, M., Schoutens, K. & Gerritsma, R. High-fidelity method for a single-step *N*-bit Toffoli gate in trapped ions. *Phys. Rev. A* **103**, 052437 (2021).
28. Figgatt, C. et al. Complete 3-qubit Grover search on a programmable quantum computer. *Nat. Commun.* **8**, 1918 (2017).
29. Marvian, I. Restrictions on realizable unitary operations imposed by symmetry and locality. *Nat. Phys.* **18**, 283–289 (2022).
30. Lloyd, S. Universal quantum simulators. *Science* **273**, 1073–1078 (1996).
31. Bullock, S. S. & Markov, I. L. Asymptotically optimal circuits for arbitrary *n*-qubit diagonal comutations. *Quantum Inf. Comput.* **4**, 27–47 (2004).
32. Efimov, V. Energy levels arising from resonant two-body forces in a three-body system. *Phys. Lett. B* **33**, 563–564 (1970).
33. Kraemer, T. et al. Evidence for Efimov quantum states in an ultracold gas of caesium atoms. *Nature* **440**, 315–318 (2006).
34. Aaij, R. et al. Observation of $J/\psi p$ resonances consistent with pentaquark states in $\Lambda_b^0 \to J/\psi k^- p$ decays. *Phys. Rev. Lett.* **115**, 072001 (2015).
35. Weimer, H., Müller, M., Lesanovsky, I., Zoller, P. & Büchler, H. P. A Rydberg quantum simulator. *Nat. Phys.* **6**, 382–388 (2010).
36. Isenhower, L., Saffman, M. & Mølmer, K. Multibit C_k NOT quantum gates via Rydberg blockade. *Quantum Inf. Process.* **10**, 755–770 (2011).
37. Levine, H. et al. Parallel implementation of high-fidelity multiqubit gates with neutral atoms. *Phys. Rev. Lett.* **123**, 170503 (2019).
38. Xing, T. H., Zhao, P. Z. & Tong, D. M. Realization of nonadiabatic holonomic multiqubit controlled gates with Rydberg atoms. *Phys. Rev. A* **104**, 012618 (2021).
39. Khazali, M. & Mølmer, K. Fast multiqubit gates by adiabatic evolution in interacting excited-state manifolds of Rydberg atoms and superconducting circuits. *Phys. Rev. X* **10**, 021054 (2020).
40. Naidon, P. & Endo, S. Efimov physics: a review. *Rep. Prog. Phys.* **80**, 056001 (2017).
41. Zahedinejad, E., Ghosh, J. & Sanders, B. C. High-fidelity single-shot Toffoli gate via quantum control. *Phys. Rev. Lett.* **114**, 200502 (2015).
42. Hill, A. D., Hodson, M. J., Didier, N. & Reagor, M. J. Realization of arbitrary doubly-controlled quantum phase gates. Preprint at *arXiv* https://doi.org/10.48550/arXiv.2108.01652 (2021).
43. Kim, Y. et al. High-fidelity three-qubit *i*Toffoli gate for fixed-frequency superconducting qubits. *Nat. Phys.* **18**, 783–788 (2022).
44. Menke, T. et al. Demonstration of tunable three-body interactions between superconducting qubits. *Phys. Rev. Lett.* **129**, 220501 (2022).
45. Cirac, J. I. & Zoller, P. Quantum computation with cold trapped ions. *Phys. Rev. Lett.* **74**, 4091–4094 (1995).
46. Monz, T. et al. Realization of the quantum Toffoli gate with trapped ions. *Phys. Rev. Lett.* **102**, 040501 (2009).
47. Goto, H. & Ichimura, K. Multiqubit controlled unitary gate by adiabatic passage with an optical cavity. *Phys. Rev. A* **70**, 012305 (2004).
48. Gambetta, F. M., Zhang, C., Hennrich, M., Lesanovsky, I. & Li, W. Long-range multibody interactions and three-body antiblockade in a trapped Rydberg ion chain. *Phys. Rev. Lett.* **125**, 133602 (2020).
49. Milburn, G., Schneider, S. & James, D. Ion trap quantum computing with warm ions. *Fortschr. Phys.* **48**, 801–810 (2000).
50. Solano, E., de Matos Filho, R. L. & Zagury, N. Deterministic Bell states and measurement of the motional state of two trapped ions. *Phys. Rev. A* **59**, R2539–R2543 (1999).
51. Burd, S. et al. Quantum amplification of boson-mediated interactions. *Nat. Phys.* **17**, 898–902 (2021).
52. Shapira, Y., Cohen, S., Akerman, N., Stern, A. & Ozeri, R. Robust two-qubit gates for trapped ions using spin-dependent squeezing. *Phys. Rev. Lett.* **130**, 030602 (2023).
53. Katz, O., Cetina, M. & Monroe, C. *N*-body interactions between trapped ion qubits via spin-dependent squeezing. *Phys. Rev. Lett.* **129**, 063603 (2022).
54. Katz, O., Cetina, M. & Monroe, C. Programmable *N*-body interactions with trapped ions. Preprint at *arXiv* https://doi.org/10.48550/arXiv.2207.10550 (2022).
55. Maunz, P. L. W. *High Optical Access Trap 2.0*. Technical Report (Sandia National Lab, 2016).
56. Egan, L. et al. Fault-tolerant control of an error-corrected qubit. *Nature* **598**, 281–286 (2021).
57. Cetina, M. et al. Control of transverse motion for quantum gates on individually addressed atomic qubits. *PRX Quantum* **3**, 010334 (2022).
58. Olmschenk, S. et al. Manipulation and detection of a trapped Yb^+ hyperfine qubit. *Phys. Rev. A* **76**, 052314 (2007).
59. Egan, L. N. *Scaling Quantum Computers with Long Chains of Trapped Ions*. PhD thesis, Univ. Maryland (2021).
60. Sørensen, A. & Mølmer, K. Entanglement and quantum computation with ions in thermal motion. *Phys. Rev. A* **62**, 022311 (2000).
61. Zhu, S.-L., Monroe, C. & Duan, L.-M. Trapped ion quantum computation with transverse phonon modes. *Phys. Rev. Lett.* **97**, 050505 (2006).
62. Sackett, C. A. et al. Experimental entanglement of four particles. *Nature* **404**, 256–259 (2000).
63. Lu, Y. et al. Global entangling gates on arbitrary ion qubits. *Nature* **572**, 363–367 (2019).
64. Pogorelov, I. et al. Compact ion-trap quantum computing demonstrator. *PRX Quantum* **2**, 020343 (2021).
65. Figgatt, C. et al. Parallel entangling operations on a universal ion-trap quantum computer. *Nature* **572**, 368–372 (2019).

66. Shapira, Y., Shaniv, R., Manovitz, T., Akerman, N. & Ozeri, R. Robust entanglement gates for trapped-ion qubits. *Phys. Rev. Lett.* **121**, 180502 (2018).
67. Wang, Y. et al. High-fidelity two-qubit gates using a microelectromechanical-system-based beam steering system for individual qubit addressing. *Phys. Rev. Lett.* **125**, 150505 (2020).
68. Leung, P. H. et al. Robust 2-qubit gates in a linear ion crystal using a frequency-modulated driving force. *Phys. Rev. Lett.* **120**, 020501 (2018).
69. Webb, A. E. et al. Resilient entangling gates for trapped ions. *Phys. Rev. Lett.* **121**, 180501 (2018).
70. Biamonte, J. et al. Quantum machine learning. *Nature* **549**, 195–202 (2017).
71. Zhou, L., Wang, S.-T., Choi, S., Pichler, H. & Lukin, M. D. Quantum approximate optimization algorithm: performance, mechanism, and implementation on near-term devices. *Phys. Rev. X* **10**, 021067 (2020).
72. Cerezo, M. et al. Variational quantum algorithms. *Nat. Rev. Phys.* **3**, 625–644 (2021).
73. Kandala, A. et al. Hardware-efficient variational quantum eigensolver for small molecules and quantum magnets. *Nature* **549**, 242–246 (2017).

Methods

Native ion–phonon interactions

We control the displacement and squeezing operations of the ions using pairs of optical Raman beams (Supplementary Fig. 1 shows the schematic). The beam that globally addresses the chain traverses an acousto-optical modulator that is simultaneously driven with two RF signals $A_+\sin(\omega_+ t+\phi_+(t))$ and $A_-\sin(\omega_- t+\phi_-(t))$ that split and shift its optical frequency into two distinct tones. We simultaneously drive both red- and blue-sideband transitions to generate displacement or squeezing operations, and set their amplitudes A_+ and A_- to be nearly equal. Control over the beatnote frequency, $\frac{1}{2}(\omega_+-\omega_-)$, of the tones with respect to the carrier transition enables selection of the driven sidebands transitions; here we address the lowest-frequency radial mode, denoted as mode number 1 with frequency ω_1, by tuning the relative detuning $\Delta=\frac{1}{2}(\omega_+-\omega_-)-\omega_1$ to be on resonance ($\Delta=0$). We modulate the amplitude of the individually addressing beams to control the amplitude of the displacement of the target zig-zag mode as well as to suppress the displacements of all the other off-resonant modes. The amplitude-shaped waveform is based on the optimal control technique[54] using a sinusoidal basis (Supplementary Fig. 2 shows an example for a single displacement stage of a three-ion chain).

The spin-dependent displacement operator on the nth ion as a function of time is given by[53]

$$D^{(n)}(\alpha(t))=\exp\left(\hat{\sigma}_{\varphi}^{(n)}(\alpha(t)\hat{a}^{\dagger}-\alpha^{*}(t)\hat{a})\right), \tag{3}$$

where $\hat{a}=\hat{q}+\mathrm{i}\hat{p}$ denotes the bosonic phonon annihilation operator of the target lowest-frequency radial mode. The time-dependent displacement is given by

$$\alpha(t)=\frac{1}{2\mathrm{i}}\eta_{n1}\int_0^t \mathrm{d}\tau \mathrm{e}^{\mathrm{i}(\Delta\tau+\delta\varphi)}\Omega_n(\tau). \tag{4}$$

Here $\Omega_n(t)$ is the Rabi frequency that can be varied up to about 1 MHz, as we independently calibrate experimentally using single-qubit rotations acting on the carrier transition. The Lamb–Dicke parameters $\eta_{n1}=0.08b_{n1}$ characterizing the coupling of the zig-zag motional mode to the nth spin include mode participation factors for the zig-zag mode (number 1) of $b_{n1}=(0.41, 0.82, 0.41)$ for the three-ion chain and $b_{n1}=(0.21, -0.67, 0.67, -0.21)$ for the four-ion chain, assuming a quadratic trapping potential along the chain axis. The applied potentials give an average spacing of about 3.7 μm between the ions to maximize coupling with the equidistant fixed-spacing optical Raman beams, for which $\omega_1=2.817$ MHz for the three-ion chain and $\omega_1=2.781$ MHz for the four-ion chain, where the radial centre-of-mass frequency in both configurations is 3.030 MHz.

The relative phase between the two RF tones $\delta\varphi=(\phi_+-\phi_-)/2$ controls the orientation of displacement in the phase space, and the common phase $\bar{\varphi}=(\phi_++\phi_--\pi)/2$ determines the orientation of the spin operator on the Bloch sphere $\hat{\sigma}_{\bar{\phi}}^{(n)}=\cos\bar{\varphi}_n\hat{\sigma}_x^{(n)}+\sin\bar{\varphi}_n\hat{\sigma}_y^{(n)}$. We nominally tune the phase $\bar{\varphi}_n=0$ to render the operator $\hat{\sigma}_{\bar{\phi}}^{(n)}=\hat{\sigma}_x^{(n)}$ as considered in the main text, and tune $\Delta=0$ to resonantly drive the lowest-frequency phonon mode and generate the edges of the rectangular-shaped trajectories whose orientation depends on the relative phase; motion along the q ($-q$) coordinate (denoted as D_q in Extended Data Fig. 1) is realized by setting the relative phase at $\delta\varphi=0$ ($\delta\varphi=\pi$) and motion along the p ($-p$) coordinate (denoted as D_p in Extended Data Fig. 1) is realized by setting $\delta\varphi=\pi/2$ ($\delta\varphi=3\pi/2$). The duration of a displacement pulse is 26 μs in the three-ion configuration and 44 μs in the four-ion configuration.

We apply squeezing operations on the zig-zag mode by tuning the relative frequency of the tones at twice the motional frequency, $\Delta=\frac{1}{2}(\omega_+-\omega_-)-2\omega_1=0$. Here we use an unmodulated square-shaped pulse (with about 1 μs for the rise time and fall time of the edges), and we find that the expected coupling to the other modes is small. This acts on the nth ion to squeeze the motion according to the operator

$$S_{\hat{\xi}}^{(n)}(t)=\mathrm{e}^{\frac{1}{2}\hat{\sigma}_{\bar{\phi}}^{(n)}\xi(t)(\hat{a}^2-\hat{a}^{\dagger 2})}, \tag{5}$$

where the projection of the spin operator is controlled by the common phase of the two tones, $\bar{\phi}=\pi+(\phi_++\phi_-)/2$. We nominally tune $\bar{\phi}=0$ so that $\hat{\sigma}_{\bar{\phi}}^{(n)}=\hat{\sigma}_x^{(n)}$. The squeezing amplitude and its orientation are, thus, given by the complex parameter

$$\xi(t)=\frac{1}{2}\eta_{n1}^2\int_0^t \mathrm{d}\tau\Omega_n(\tau)\mathrm{e}^{\mathrm{i}(\Delta\tau+\delta\phi)}. \tag{6}$$

We tune $\Delta=0$ to resonantly drive the zig-zag mode and control the direction in the motional phase space that is squeezed using $\delta\phi=(\phi_+-\phi_-)/2$. The direction of squeezing in the experiment is aligned with the q coordinate, with squeezing (anti-squeezing) corresponding to $\delta\phi=0(\pi)$. The duration of a squeezing pulse is about 29 μs in the three-ion configuration and about 49 μs in the four-ion configuration. In particular, the control over the phases $\delta\varphi$ and $\delta\phi$ (determining the direction of displacement and squeezing operations, respectively) depends only on the relative phases $\phi_+-\phi_-$ of the two RF signals that are fed into one of the acousto-optical modulators, and do not depend on the relative optical phases of the Raman beams.

We implement single-qubit rotations using a composite pulse sequence (SK1 sequence[74]) to implement the unitary operation

$$R_{\theta}^{(n)}(\chi)=\exp\left(-\mathrm{i}\frac{\chi}{2}\hat{\sigma}_{\theta}^{(n)}\right) \tag{7}$$

on the nth spin by driving a single tone of the global beam ($A_-=0$) on resonance with the carrier transition such that $\theta=\phi_+$. Each single-qubit gate takes 12.7 μs. We use these single-qubit operations for the preparation of the initial state along the x axis and for echo pulses $R_0^{(n)}(\pm\pi)$ that commute with the spin operators in the circuit and suppressing effects of small uncompensated light shifts.

Experimental calibration

We verify the value of $\bar{\varphi}=0$ by running a short sequence $R_{\theta}^{(n)}\left(\frac{\pi}{2}\right)D^{(n)}(\alpha)R_{\theta}^{(n)}\left(-\frac{\pi}{2}\right)$ on the target spin initially in state $|\downarrow_z\rangle$ and for variable rotation axis θ. The angle θ_0 for which the spin-flip probability is minimal gives $\bar{\varphi}=\theta_0+\frac{\pi}{2}$. Similarly, we verify the value of $\bar{\phi}=0$ by running a short sequence $R_{\theta}^{(n)}\left(\frac{\pi}{2}\right)S_{\xi}^{(n)}R_{\theta}^{(n)}\left(-\frac{\pi}{2}\right)$on the target spin initially in state $|\downarrow_z\rangle$, and find that $\bar{\varphi}=\theta_0$.

We verify the relative orientation of the displacement and squeezing operations, $\delta\varphi$ with respect to $\delta\phi$, by measuring the spin-flip probability of the edge ions for the squeezed rectangle phase gate by the sequence in Extended Data Fig. 1b for the initial state $\left|\downarrow_z^{(1)}\downarrow_x^{(2)}\downarrow_z^{(3)}\right\rangle$ and the nominal value of $\delta\varphi=0$ but for different values of $\delta\phi$. For small displacement and squeezing ($\Phi_0\mathrm{e}^{\xi}<\frac{\pi}{2}$), the spin-flip probability is minimized for $\delta\phi=0$ and is given by $p_{\mathrm{a}}=\sin^2(\mathrm{e}^{-\xi}\Phi_0)$, whereas it is maximized for $\delta\phi=\pi$ and is given $p_{\mathrm{b}}=\sin^2(\mathrm{e}^{-\xi}\Phi_0)$. The measured values of p_{a} and p_{b} can determine Φ_0 and ξ.

We compensate for light-induced shifts generated during the displacement and squeezing operations by tuning the relative amplitude imbalance of the two tones $|A_+-A_-|/|A_++A_-|$ at the level of about 1%. The imbalance applied during the squeezing and displacement operations is independently tuned to account for different shifts, for example, from residual coupling to Zeeman states outside of the space of the spin qubits and detuned by ±4.2 MHz from the carrier spin-flip transition. The orientation of the magnetic field is also tuned to suppress the Zeeman transition amplitudes.

We routinely calibrate for drifts in the motional frequency of the oscillator by driving sequences that combine $D^{(n)}(\alpha)D^{(n)}(-\alpha)$ and scanning for the motional frequency Δ (Supplementary Fig. 3a). Here we implement $D^{(n)}(-\alpha)$ by applying the pulse $D^{(n)}(\alpha)$ and shifting the motional phase by $\delta\varphi \to \delta\varphi + \pi$, which manifests the inverse of the displacement operation only if the driving is resonant ($\Delta = 0$). When the displacement is driven off-resonantly, the operation is not reversed and residual coupling between the spin and phonons leads to a non-zero spin-flip probability, which allows the calibration of the motional frequency to better than 100 Hz. Similarly, the operations $S_{\xi}^{(n)}S_{-\xi}^{(n)}$, where $S_{-\xi}^{(n)}$ are realized by advancing $\delta\phi$ by π, give a similar dependence on motional frequency. We generated a composite sequence that uses these operations and allows for an efficient check of the motional frequency (Supplementary Fig. 3b). Additional details and characterizations of our experimental setup can be found elsewhere[3,56,59].

Data availability

Source data are provided with this paper. Other data that support the findings of this study are available from the corresponding authors on reasonable request.

References

74. Brown, K. R., Harrow, A. W. & Chuang, I. L. Arbitrarily accurate composite pulse sequences. *Phys. Rev. A* **70**, 052318 (2004).

Acknowledgements

We thank A. Schuckert for useful comments. This work is supported by the ARO through the IARPA LogiQ program; the NSF STAQ and QLCI programs; the DOE QSA program; the AFOSR MURIs on Dissipation Engineering in Open Quantum Systems, Quantum Measurement/Verification and Quantum Interactive Protocols; the ARO MURI on Modular Quantum Circuits; and the DOE HEP QuantISED Program.

Author contributions

All authors contributed to the experimental design, construction and discussions and wrote the manuscript. O.K. collected the data, and O.K. and L.F. analysed the results. L.F. produced Fig. 1. O.K. produced Figs. 2–4.

Competing interests

O.K., L.F. and A.R. declare that they have no competing interests. M.C. is a co-inventor of the intellectual property that is licensed by the University of Maryland to IonQ, Inc. C.M. is a co-founder and chief scientist at IonQ, Inc.

Additional information

Extended data is available for this paper at https://doi.org/10.1038/s41567-023-02102-7.

Supplementary information The online version contains supplementary material available at https://doi.org/10.1038/s41567-023-02102-7.

Correspondence and requests for materials should be addressed to Or Katz or Lei Feng.

Peer review information *Nature Physics* thanks Christian Schmiegelow and the other, anonymous, reviewer(s) for their contribution to the peer review of this work.

https://doi.org/10.1038/s41567-023-02102-7

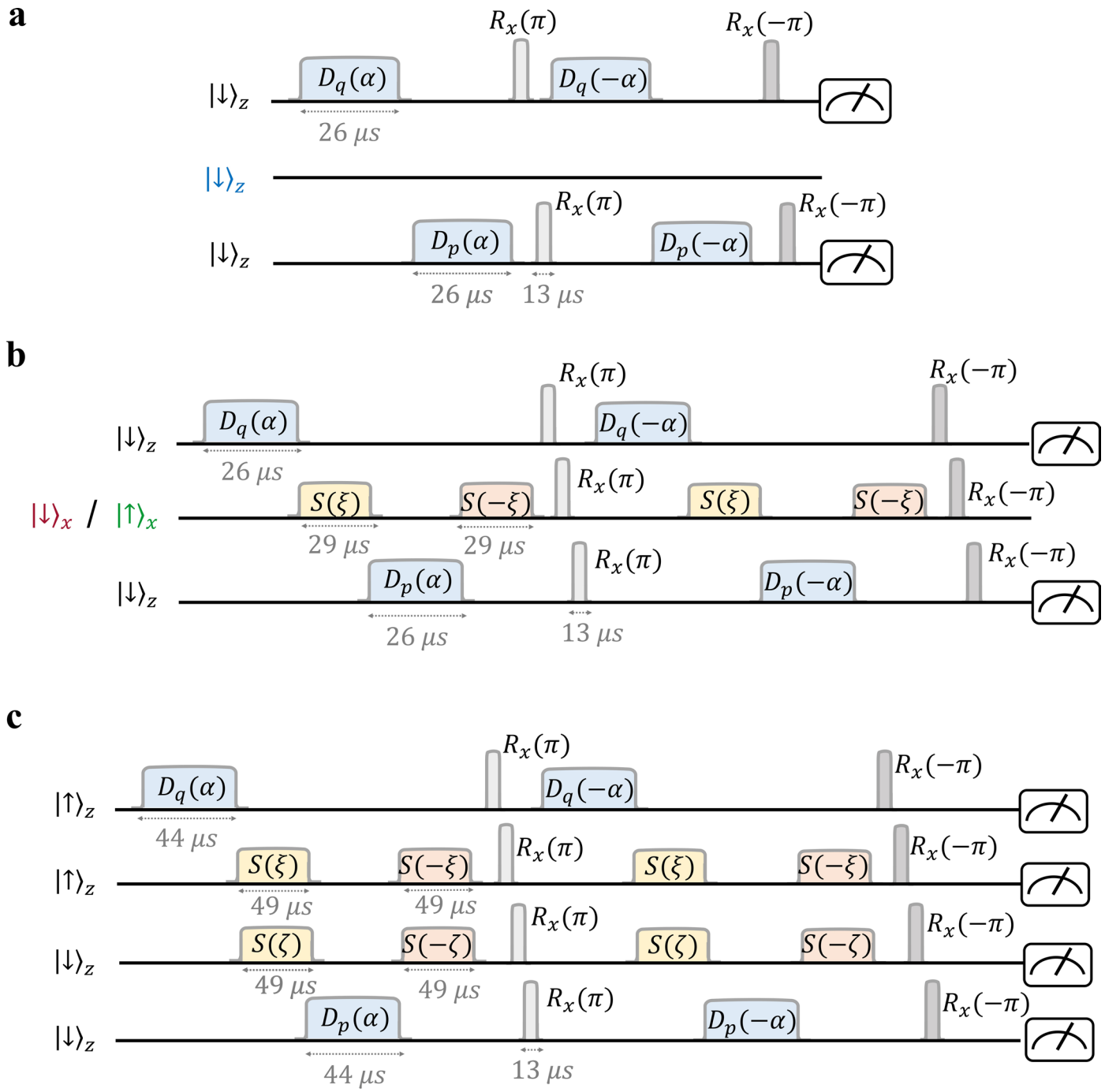

Extended Data Fig. 1 | Experimental sequences. a, Sequence of displacement operations acting on the two edge ions and composing the MS interaction, enclosing a closed rectangular loop in phase-space and generating the evolution in Fig. 2a. **b**, Superimposing spin-dependent squeezing operations on the second spin scales the displacement generated by the third spin by a factor $\exp(\hat{\sigma}_x^{(2)}\xi)$ and consequently also the enclosed phase-space area. This sequence was applied to the configurations in Fig. 2b–c and in Fig. 3 and Fig. 4a. **c**, Displacement of the edge two spins and simultaneous squeezing of the middle spins for the four ions configuration presented in Fig. 4b. The simultaneous squeezing scales the displacement generated by the fourth spin by a spin-dependent factor $\exp(\hat{\sigma}_x^{(2)}\xi + \hat{\sigma}_x^{(3)}\zeta)$ as seen from the identity $S^{(m)}(-\xi)D_p^{(n)}(\pm\alpha)S^{(m)}(\xi) = D_p^{(n)}(\pm e^{\hat{\sigma}_x^{(m)}\xi}\alpha)$. The operators $D_p^{(n)}(\pm\alpha)$ and $D_q^{(n)}(\pm\alpha)$ denote displacement of the target phonon mode via the nth ion by $\pm\alpha$ along the p and q coordinates respectively. $S^{(m)}(\pm\xi)$ denotes the squeezing operator acting on ion m and $R_\theta^{(n)}(\pm\pi)$ denotes short single-qubit π-pulses acting on the n th ion, which commute with the spin-dependent displacement operations and which correct for slowly-varying uncompensated Stark shifts without altering the target state. See Methods for further details.